Journal of Polymer Science

SPECIAL ISSUE Special Issue in Celebration of Prof. Sindee Simon's 65th Birthday

WILEY

JOURNAL OF POLYMER SCIENCE

RESEARCH ARTICLE

Predicting Cure Evolution and Thermal Endurance of a Highly Filled Epoxy Underfill for Advanced Packaging

Ryan Giang[1,2] | Ran Tao[1,3] | Elena Moukhina[4] | Amanda L. Forster[1] | Tae Joon Cho[1] | Polette J. Centellas[1] | Stian K. Romberg[1,5] | Zois Tsinas[1,6] | Christopher L. Soles[1]

[1]Material Measurement Laboratory, National Institute of Standards and Technology, Gaithersburg, Maryland, USA | [2]Department of Chemical and Nano Engineering, University of California San Diego, La Jolla, California, USA | [3]Department of Chemical and Biomolecular Engineering, North Carolina State University, Raleigh, North Carolina, USA | [4]NETZSCH-Gerätebau GmbH, Selb, Germany | [5]Department of Mechanical and Aerospace Engineering, University of Tennessee, Knoxville, Tennessee, USA | [6]Theiss Research, La Jolla, California, USA

Correspondence: Ran Tao (ran.tao@nist.gov)

Received: 11 May 2026 | **Revised:** 19 July 2026 | **Accepted:** 20 July 2026

Keywords: advanced electronic packaging | cure kinetics | differential scanning calorimetry | diffusion-controlled reaction | epoxy underfill | isoconversional analysis | thermal endurance | thermogravimetric analysis | vitrification

ABSTRACT

Epoxy underfill materials are critical to advanced semiconductor packaging by enhancing mechanical integrity, redistributing thermomechanical stresses, and improving solder-joint reliability in flip-chip and other fine-pitch interconnect architectures. Their performance is strongly influenced by cure evolution during processing and thermal stability during service, making quantitative evaluation important for process optimization and long-term reliability assessment. The cure kinetics and thermal degradation behavior of a highly-filled epoxy underfill were investigated using differential scanning calorimetry (DSC), thermogravimetric analysis (TGA), and diffusion-incorporated kinetic modeling. Isoconversional analysis showed that the apparent activation energy varied with conversion and increased sharply at high conversion, indicating multi-step cure behavior and diffusion control. A two-step modified Kamal–Sourour model incorporating diffusion control in the second step improved prediction of conversion after vitrification and was used to predict cure evolution under a designed oven cure schedule, which achieved nearly complete cure. Cryomilling improved TGA reproducibility without causing detectable chemical changes. Analysis following the ASTM E1641/E1877 protocols revealed a strong temperature dependence of estimated thermal endurance based on a 5% mass-loss criterion under nitrogen. Together, the results provide a quantitative framework for predicting cure evolution under practical thermal schedules, evaluating late-stage diffusion effects, and estimating degradation-based thermal endurance for highly-filled industrial thermosets.

1 | Introduction

Epoxy underfill materials are widely used in advanced electronic packaging to improve mechanical integrity, redistribute thermomechanical stresses, and enhance solder-joint reliability. They are used as encapsulants that fill the gap between the semiconductor die and the substrate, particularly in flip-chip and other fine-pitch interconnect architectures [1]. By encapsulating the interconnect region, underfill helps protect solder joints from fatigue, cracking, delamination, and environmental damage during service. Their performance depends not only on the final epoxy network structure after processing [2], but also on the cure path itself, since the evolution of conversion, glass transition temperature, and residual stresses [3, 4] during processing can strongly influence long-term reliability [5]. A quantitative understanding of cure evolution is important for both fundamental insight and industrial practice, supporting process optimization and materials qualification [6]. For commercial

underfill formulations used at industry scale, the combined effects of multi-step cure behavior arising from complex resin chemistry and high inorganic filler loading make it difficult to predict cure completion using simplified kinetic descriptions commonly employed in industry practice [7–10].

Kinetic analysis of thermoset curing is commonly performed using model-free and model-based approaches. Isoconversional methods are useful for assessing changes in activation energy and thus whether a single-step kinetic description is appropriate, whereas model-based approaches can be used to describe the full reaction path [11]. For many epoxy systems, however, the apparent activation energy varies with conversion [12–14], indicating that multiple reaction steps may be involved [15]. Furthermore, at high conversion, vitrification reduces molecular mobility and diffusion limitations increasingly suppress the reaction rate [16, 17]. Under these conditions, purely chemically controlled models may adequately describe the early and intermediate stages of cure but often fail to capture the late-stage regime. A kinetic description that accounts for both multi-step cure behavior and diffusion limitations is therefore needed to predict cure evolution across all cure stages relevant to practical processing conditions.

In addition to cure kinetics, thermal stability is also an important consideration for underfill materials used in demanding service environments. For example, electronic components in an automotive engine compartment experience an ambient service temperature of around 150°C, and operating temperatures can range from 175°C to 200°C [18]. Thermal degradation behavior of epoxy underfill is influenced by its chemical composition, including both the polymer network and inorganic filler content. Dynamic thermogravimetric analysis (TGA) [19] performed at multiple heating rates, together with ASTM E1641 and ASTM E1877 methods [20, 21], provides a practical route for estimating apparent activation energy from degradation-based kinetic analysis and for assessing temperature-dependent thermal endurance [22]. For highly filled thermosets, reproducible TGA measurements require consistent sample preparation because heat and mass transfer during decomposition are sensitive to sample geometry [20]. Establishing a reproducible method for thermal degradation analysis is therefore essential for obtaining meaningful kinetic parameters and lifetime predictions.

The cure kinetics and thermal degradation behavior of a highly filled epoxy underfill have been investigated using dynamic differential scanning calorimetry (DSC), dynamic TGA, and kinetic modeling. Model-free analysis was first used to evaluate the conversion dependence of the apparent activation energy, and a two-step modified Kamal–Sourour model with diffusion control was then used to describe cure evolution and predict conversion under a practical oven cure schedule. To evaluate thermal stability, cured samples were cryomilled to improve TGA reproducibility, and the dynamic TGA data were analyzed using ASTM E1641 and ASTM E1877 to estimate the apparent activation energy and temperature-dependent thermal endurance. Together, these results provide a quantitative framework for linking cure schedule design, diffusion-incorporated cure kinetics modeling, and degradation-based lifetime assessment for highly filled epoxy underfill systems used in advanced packaging applications.

2 | Experimental

2.1 | Materials

A commercial epoxy underfill, Loctite ECCOBOND UF 1173, was purchased from Henkel Corporation.[1] It is a one-part, silica-filled, epoxy-based thermosetting resin system widely used in industrial processes for flip-chip and fine-pitch device encapsulation. The liquid underfill material was shipped on dry ice from the manufacturer and stored at −40°C upon receipt prior to use.

2.2 | DSC Measurements

A TA Instruments Discovery DSC 2500 differential scanning calorimeter with an RCS 90 intracooler maintained at −90°C and nitrogen purge gas was used to study the cure kinetics of the commercial underfill. The masses of DSC samples ranged from 10 to 20 mg. After removal from the −40°C freezer, the liquid underfill was allowed to equilibrate to room temperature for 10 min before being loaded into 40 μL hermetic aluminum pans and sealed for measurement. The DSC temperature was calibrated using indium, tin, and lead at 10 K min^{-1}, and the heat flow was calibrated with indium. The standard uncertainties for temperature and heat flow are estimated to be ±1% and ±3%, respectively.

For dynamic DSC experiments, the uncured samples were heated from 30°C to 300°C at constant heating rates of 0.6, 1, 3, 5, 10, and 20°C min^{-1}. The samples were then quenched to −30°C at a rate of approximately 50°C min^{-1} after the first heating scan, and a second heating scan up to 300°C at 10°C min^{-1} was performed to measure the cured material T_g and any residual heat. To measure the T_g of the uncured material, a broader temperature range, from −90°C to 300°C, was used for the first heating scan.

2.3 | Preparation and Processing of Cured Epoxy Underfill

The uncured liquid material was deposited onto a glass substrate laminated with a fluorinated ethylene propylene (FEP) protective film with an aluminum support backing. It was then placed in a forced-air oven (Cascade TEK model TFO-3) and cured using a two-step schedule: first at 150°C for 30 min, followed by 185°C for 30 min. A thermocouple was directly attached to the surface of the glass substrate to monitor the substrate temperature, and the temperature data were recorded every 100 ms throughout the thermal curing process. The oven was allowed to equilibrate to room temperature before retrieving the cured samples.

The cured samples were removed from the glass substrate and cut into approximately 50 mm^2 pieces (1–2 mm thick) using a razor blade. The pieces were then weighed to obtain a total mass of approximately 4 g. Cryogenic milling (cryomilling) was performed using a Retsch CryoMill equipped with a stainless-steel grinding jar with a 25 mm diameter milling ball continuously cooled with liquid nitrogen from an autofill system to maintain a cryogenic temperature of −196°C. The milling procedure

consisted of an initial 15 min precooling step at 5 Hz, followed by 30 grinding cycles of 2 min each at 30 Hz, for a total grinding duration of 60 min. A 2 min aftercooling step at 5 Hz was applied after each cycle. The jar was opened after full equilibration to ambient temperature to minimize moisture condensation. The total sample mass (≈4 g) was maintained after cryomilling. Particle size distribution of the cryomilled powder was characterized using a laser diffraction particle size analyzer (Horiba Partica LA-950V2). The powder was dispersed in 0.01% (w/v) aqueous Tergitol 15-S-15 (Sigma-Aldrich) at a 0.1% (w/v) solids concentration using probe ultrasonication. This stock suspension was then diluted to an appropriate concentration for laser diffraction measurements. Fourier transform infrared (FTIR) spectroscopy was used to evaluate the effect of cryomilling on the chemical structure of the cured material. Hand-cut bulk and cryomilled powder samples were measured in triplicate, and spectra were acquired between 4000 and 800 cm^{-1} at a resolution of 4 cm^{-1} using a Thermo Scientific Nicolet iS50 FTIR spectrometer equipped with a Nicolet iTX diamond attenuated total reflectance (ATR) accessory. FTIR spectra were post-processed for baseline correction using Origin Pro software.

2.4 | TGA Measurements

Thermal stability and decomposition kinetics of the cured underfill were evaluated using a TA Instruments Discovery TGA 550 thermogravimetric analyzer under a nitrogen atmosphere. Sample masses ranged from 10 to 20 mg. Cryomilled underfill samples were loaded into 100 μL alumina pans for measurement. For the hand-cut bulk sample, a single piece of material weighing 15 to 20 mg was measured from 30°C to 800°C at heating rates of 1, 3, 5, 10, and 20°C min^{-1}. For the cryomilled sample, a two-step procedure was used. In the first run, the samples were heated from 30°C to 130°C at 10°C min^{-1}, followed by a 30 min isotherm hold to remove residual moisture (pre-drying step) [23]. A second dynamic heating run was performed from 30°C to 800°C at heating rates of 1, 3, 5, 10, and 20°C min^{-1}. Thermal degradation temperatures were determined from the second dynamic heating run. The first derivative of the TGA curve (derivative thermogravimetry or DTG), $d(\text{mass})/dT$, was also evaluated.

3 | Results and Discussion

3.1 | Cure Kinetics

Figure 1 shows the DSC heat flow curves, scaled by β_{ref}/β (where β is the heating rate $\beta = dT/dt$ and $\beta_{ref} = 10\,K\,min^{-1}$), for the uncured samples measured at different heating rates ranging from 0.6 to 20 K min^{-1}. This scaling provides a more effective way to compare DSC results at different heating rates with the same sensitivity [7]. An exothermic peak corresponding to the curing reaction is observed for all curves. As the heating rate increases, the reaction exotherm shifts to higher temperatures due to the reduced reaction time available at a given temperature. Although each curve appears to display a single exothermic peak, both the height and width of the reaction peaks vary noticeably with heating rate: at low rates (0.6 and 1 K min^{-1}) the exotherms are sharp and narrow, whereas at higher rates (3 to 20 K min^{-1}) they broaden in width and decrease in intensity. Furthermore, the peaks are asymmetric, exhibiting a distinct tail on the high-temperature side, as shown in the enlarged view in Figure S1, especially for slower heating rates. Taken together, the pronounced peak broadening, intensity variation, and asymmetry clearly indicate that the curing does not follow a single-step kinetic process, but instead involves overlapping multi-step reactions and/or a rate-limiting stage that becomes more prominent at higher conversion. Importantly, the apparent absence of peak shoulders or multiple peaks in the DSC curves should not be interpreted as evidence of single-step kinetics [24].

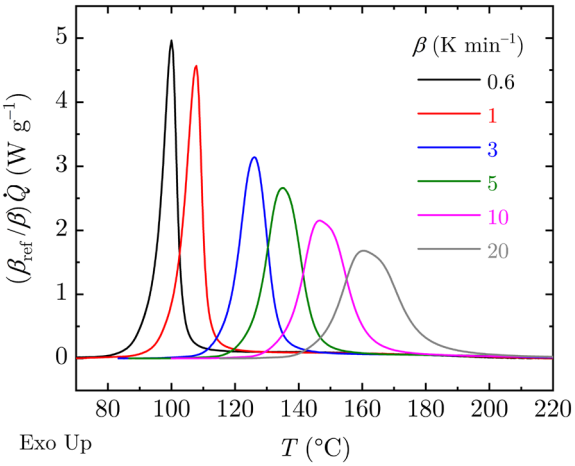

FIGURE 1 | Dynamic DSC heat flow curves for the uncured underfill material measured at different heating rates (β). Heat flow ($\dot{Q}$) is scaled by (β_{ref}/β), where β_{ref} is taken to be 10 K min^{-1}.

No residual heat was observed during the second heating scan for all heating rates, which confirmed the fully cured state of the material (Figure S2). It is also noted that T_g measurements by conventional DSC for cured, highly filled thermosets can be challenging [7]. The value of ΔC_p at T_g reflects the amount of polymer contributing to the mobility and configurational entropy of the network. As the crosslink density increases, the fraction of mobile, disordered polymer chains decreases, leading to a minimal step change in the heat flow curve. As shown in Figure S2, $\Delta C_{p\infty}$ is only weakly resolved, with a value of 0.05 J g^{-1} K^{-1}. Other techniques, such as temperature-modulated DSC, may be valuable for measuring T_g in partially cured, highly filled thermosets [14].

3.2 | Model-Free Kinetic Analysis

To better discern the reaction steps, a more rigorous approach is to evaluate the apparent activation energy (E) from the temperature dependence of the reaction rate using single-step kinetic analysis. Isoconversional analysis enables estimation of E without assuming a specific kinetic model and is therefore often referred to as a 'model-free' approach. This approach assumes that, at fixed conversion α, the reaction rate depends only on temperature and is described by the kinetic equation $d\alpha/dt = k(T)f(\alpha)$ with an Arrhenius-type rate constant $k(T) = A\exp(-E/RT)$. Here we use the Friedman method [25],

which applies the isoconversional principle to the differential form of the rate equation shown below:

$$\ln\left(\frac{d\alpha}{dt}\right)_{\alpha,i} = \ln\left[A_\alpha \cdot f(\alpha)\right] - \frac{E_\alpha}{RT_{\alpha,i}} \quad (1)$$

where the subscript α denotes the values at a given conversion, i stands for the data from the ith temperature program, A is the conversion-specific pre-exponential factor, and R is the gas constant. Figure 2a shows Friedman plots of $\ln(d\alpha/dt)$ versus $1000/T$ from six dynamic heating runs at selected conversions from $\alpha = 0.02$ to 0.98. Linear fits to the isoconversional data across different heating rates yield slopes of $(-E_\alpha/R)$ at each α, as described by Equation (1). The nearly parallel lines for $\alpha \leq 0.7$ contrast with the steeper slopes at higher conversion (e.g., $\alpha \geq 0.8$), indicating an increase in E. Additionally, at the start of the reaction, the slope of the experimental data in the Friedman plot is steeper than that of the isoconversional lines, indicating the initial reaction is of an accelerating (autocatalytic) type [26, 27].

The resulting E values are plotted in Figure 2b. The activation energy decreases slightly from an initial value of $\approx$75.7 kJ mol^{-1} at low conversion ($\alpha \leq 0.1$) to a shallow minimum of $\approx$49.2 kJ mol^{-1} near $\alpha \approx 0.58$, followed by a sharp increase for $\alpha \geq 0.75$, reaching a peak value of $\approx$208.0 kJ mol^{-1} around $\alpha = 0.95$ before final cure. According to the quantitative criterion that variation in E is insignificant when the difference between its maximum and minimum values is less than 20% of the average [24], the activation energy can be considered essentially constant over $\alpha = 0.33$–0.73, with an average value of 52.5 kJ mol^{-1}. The non-constant E, varying from 75.7 to 52.5 kJ mol^{-1} and then to 208.0 kJ mol^{-1}, especially the upturn at high conversion, provides quantitative evidence of changes in reaction mechanism and underlying multi-step kinetics. Furthermore, the error bars remain small in the intermediate-conversion regime but increase markedly for $\alpha \geq 0.75$, with values of E exceeding 200 kJ mol^{-1}, indicating the reaction becomes progressively diffusion controlled as vitrification occurs. Similar behavior, characterized by an increase in E accompanied by rapidly growing uncertainties at high conversion, has been reported for epoxy systems exhibiting partial diffusion control in model-free analyses [13, 28, 29]. Several studies have also reported similarly high activation energy values, up to 200–300 kJ mol^{-1}, upon vitrification [13, 28, 30].

3.3 | Model-Based Kinetic Analysis

Once multi-step kinetic behavior is identified, the next step is to construct a kinetic model with the minimum necessary number of reaction steps and adjustable parameters, as recommended by the International Confederation for Thermal Analysis and Calorimetry (ICTAC) [24]. A two-step consecutive process, A → B → C, was therefore considered. Each step i is described by a modified Kamal–Sourour model [31] of nth order with m-power autocatalytic reaction:

$$\frac{d\alpha_i}{dt} = A_{1,i}\exp\left(-\frac{E_i}{RT}\right)\left(1-\alpha_i\right)^{n_i}\left(1+A_{2,i}\alpha_i^{m_i}\right) \quad (2)$$

and the overall degree of conversion is given by

$$\alpha = w_1\alpha_1 + w_2\alpha_2 \quad (3)$$

where w_i is the contribution of each step as $w_i = \Delta H_i / \sum \Delta H_i$ and $\sum w_i = 1$. Here, ΔH_i is the total reaction enthalpy of step i from the heat flow measured by the DSC as $\Delta H_i = \frac{1}{\beta}\int_{T_0}^{T_{end}} \dot{Q}_i(T)dT$, where T_0 is a temperature below the onset of the curing reaction and T_{end} is the temperature after completion of the reaction. The heat flow $\dot{Q}_i$(T) corresponds to the heat flow of individual reaction step i, and the total measured heat flow $\dot{Q}(T)$ is the sum of heat flows of all individual reaction steps $\dot{Q}(T) = \sum \dot{Q}_i(T)$. The degree of cure

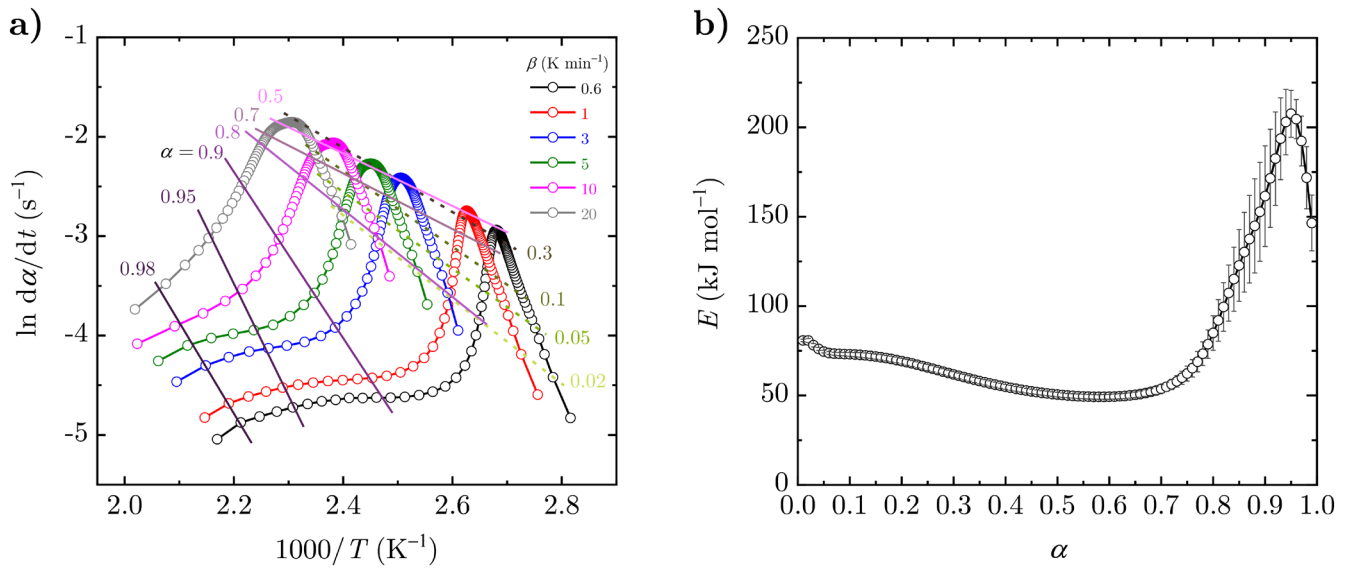

FIGURE 2 | (a) Friedman analysis of the dynamic DSC data at different heating rates (β). The lines represent isoconversional lines at various conversions (α), as indicated with slopes equal to $(-E_\alpha/R)$. Dashed lines correspond to $\alpha = 0.02$–0.3, and solid lines correspond to $\alpha = 0.5$–0.95. View in color for best clarity. (b) Apparent activation energy (E) as a function of conversion determined using the Friedman isoconversional method.

(or conversion) of the ith step, α_i, is directly correlated with the measured heat flow during the reaction: $\alpha_i = \Delta H_{T,i} / \Delta H_i$, where $\Delta H_{T,i} = \frac{1}{\beta}\int_{T_0}^{T} \dot{Q}_i(T)dT$ is the partial reaction enthalpy of the i-th step up to temperature T. The modeling was performed using the Netzsch Kinetics Neo software (version 3.5.1.9) by minimizing the least-squares error between the experimentally measured and calculated conversion values. Because of the high nonlinearity of the reaction model, it is important to use initial parameter estimates that are reasonably close to their true values for parameter optimization. Otherwise, nonlinear least-squares fitting may converge to a local rather than the global minimum, resulting in erroneous kinetic parameters regardless of the amount of data used [8, 24]. The activation energy values from the model-free analysis can serve as reliable initial estimates for this purpose.

Figure 3 shows the fitted results as solid lines and the conversion values obtained from the DSC data as symbols. The best fits are listed in Table S1. For all heating rates, the α–T profile exhibits a sigmoidal shape characteristic of thermoset curing upon dynamic heating scan [9, 11]. The two-step autocatalytic model (Equations 2 and 3) without diffusion-controlled kinetics provides a reasonable description of the conversion curves, capturing the initial acceleration and the rapid rise through intermediate conversion across all heating rates; however, it systematically overestimates the conversion at high α as the reaction gradually approaches full cure. Figure S3 compares the conversion rate $d\alpha / dt$ as a function of temperature for the 0.6 and 1 K min^{-1} scans. The results indicate that the actual reaction rate is more strongly suppressed at late stages than would be expected from purely chemically controlled kinetics, consistent with the onset of diffusion control, which slows the overall reaction rate. As a result, the model without diffusion overestimates the conversion at high α in Figure 3. Additionally, as discussed earlier, the large errors in the activation energy, as well as the high E values at high conversion from the isoconversional analysis (Figure 2b), also indicate a shift from predominantly chemically controlled curing to a mobility-limited regime (e.g., vitrification).

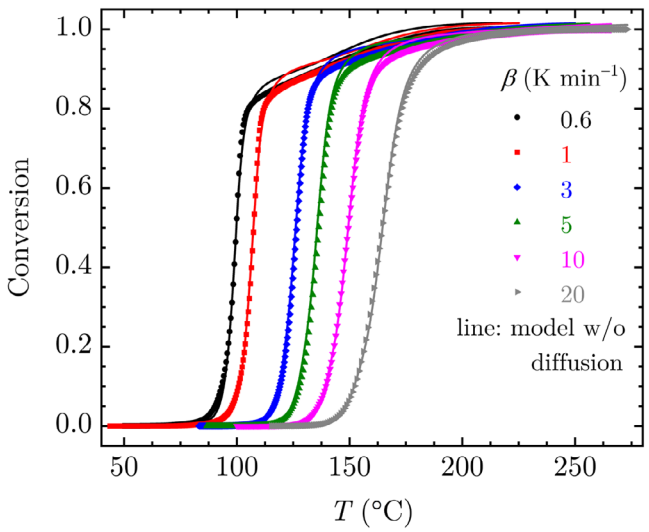

FIGURE 3 | Degree of cure (α) as a function of temperature at different heating rates (β). The symbols represent experimental data, and solid lines represent the best fits to a two-step reaction described by the modified Kamal–Sourour model (Equations 2 and 3).

For epoxy systems, it is well known that partial diffusion control arises once T_g approaches the reaction temperature. This concept has been described by the time–temperature–transformation (TTT) diagram, where the vitrification line intersects the cure path at high conversion during isothermal cure [6, 32]. Upon dynamic heating, this effect is most pronounced at low heating rates, where the progressively increasing T_g surpasses the cure temperature under a slow, linear heating profile. The influence of heating rate on the curing progression due to vitrification-induced diffusion control has been widely reported in the literature [14, 28, 33, 34].

After vitrification, diffusion becomes increasingly important. The time scale of the overall reaction can be viewed as the sum of the time scales for the chemical reaction and for diffusion. The effect of the diffusion control can be incorporated into the reaction kinetics by modifying the effective rate constant [16, 30, 35], following the Rabinowitch equation: [36]

$$k_{\text{eff}}^{-1} = k_{\text{r}}^{-1} + k_{\text{d}}^{-1} \tag{4}$$

where k_{eff}, k_{r}, and k_{d} denote the effective, reaction, and diffusion rate constants, respectively. The reaction rate constant k_{r} follows the Arrhenius temperature dependence $k_{\text{r},i}(T) = A_i \exp(-E_i / RT)$. For $T \geq T_g$, the diffusion rate constant can be considered inversely proportional to the polymer relaxation time, which is described by the well-known Williams–Landel–Ferry (WLF) equation: [37]

$$k_{\text{d}}(T) = k_0 \exp\left[\frac{C_1(T - T_g)}{C_2 + (T - T_g)}\right] \tag{5}$$

For $T < T_g$, the diffusion rate constant follows the Arrhenius form:

$$k_{\text{d}}(T) = k_0 \exp\left[-\frac{E}{R}\left(\frac{1}{T} - \frac{1}{T_g}\right)\right] \tag{6}$$

where k_0 is the reaction rate constant at $T = T_g$, and $E / R = \left(C_1 T_g^2\right) / C_2$. As the reaction proceeds, the value of T_g increases nonlinearly with conversion and follows the DiBenedetto equation: [38]

$$T_g(\alpha) = T_{g0} + \frac{(T_{g\infty} - T_{g0})\lambda\alpha}{1 - (1 - \lambda)\alpha} \tag{7}$$

where T_{g0} and $T_{g\infty}$ are the glass transition temperatures of the uncured and fully cured underfill, respectively ($T_{g0} = -47.5$°C and $T_{g\infty} = 171.0$°C). The parameter $\lambda = 0.4$ is taken as the theoretical ratio $\Delta C_{p\infty} / \Delta C_{p0}$, as proposed by Pascault and Williams [17], where $\Delta C_{p\infty}$ and ΔC_{p0} are heat capacity differences between the glassy and rubbery states at T_g for the fully cured and uncured materials, respectively. A plot of T_g versus α is shown in Figure S4.

Modeling of the overall reaction (Equations 2 and 3) incorporating diffusion control in the second reaction step via the modified rate constant (Equations 4–7), was performed using the Netzsch Kinetics Neo software (version 3.5.1.9). The best fit kinetic parameters are listed in Table 1. Figure 4 shows conversion as a function of temperature for the diffusion-incorporated

TABLE 1 | Kinetic parameters for a two-step modified Kamal–Sourour model with diffusion control included in the second step.

Parameter	First step	Second step
E (kJ mol^{-1})	75.7	52.5
$\ln(A_1)$ (s^{-1})	5.87	4.61
n	0.24	1.69
$\ln(A_2)$ (s^{-1})	2.16	0.57
m	0.69	1.72
$\ln(k_{diff})$	—	−6.28
C_1	—	17.78
C_2 (K)	—	23.20
w_i	0.07	0.93

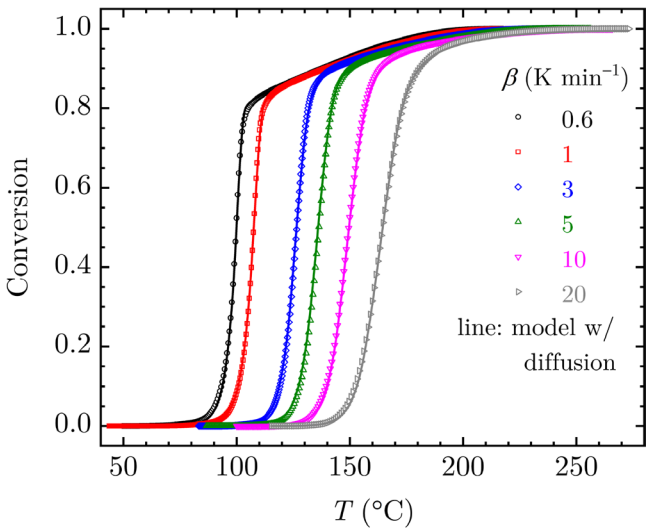

FIGURE 4 | Degree of cure (α) as a function of temperature at different heating rates (β). The symbols represent experimental data, and the lines represent best fits to a two-step reaction described by a modified Kamal–Sourour model, with diffusion control included in the second step (Equations 4–7).

model. The model predictions (lines) are in excellent agreement with experimental data (symbols) across the entire conversion range. A closer examination of the reaction rate profiles at the two lowest heating rates (Figure S5) shows that, compared with Figure S3, the diffusion-incorporated model reproduces the high-temperature shoulder associated with the onset of vitrification, leading to improved predictions at high conversion. We also note that, unlike gelation, vitrification is not an isoconversional event. The onset of vitrification, as indicated by the deviation of the model from the data in Figure 3, shifts to higher conversion with increasing heating rate. Because vitrification can occur over a wide range of conversions depending on the temperature program [33], it may be observed only at slow heating rates and may not occur at faster rates [34]. Therefore, dynamic heating DSC scans over a wide range of heating rates, especially at slow heating rates

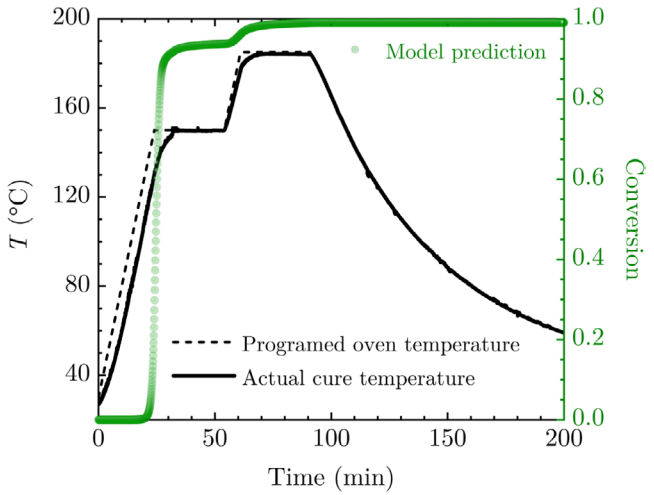

FIGURE 5 | Comparison of the programmed oven temperature versus the sample temperature during the scheduled cure (left y-axis). Also shown is the model-predicted conversion following the actual cure temperature using the same model and parameters as in Figure 4 (right y-axis).

that can reveal diffusion effects, are important for careful cure kinetics analysis.

The kinetic model can then be used to simulate conversion for any temperature program. Figure 5 shows the temperature profile following the designed cure schedule. The programmed oven temperature (dashed line) follows a first ramp from 30°C to 150°C at 5°C min^{-1}, an isothermal hold for 30 min, a second ramp to 185°C at 5°C min^{-1}, and a final 30 min hold. The actual cure temperature experienced by the sample/substrate is shown by the solid line, as measured using a thermocouple attached directly to the surface of the glass substrate in the oven. After the scheduled cure, the sample is allowed to cool to room temperature before being removed from the oven for subsequent measurements.

As expected for oven-based cure, the sample temperature does not follow the setpoint perfectly during transients: the measured temperature lags behind the programmed ramp, and step changes appear more gradual, owing to finite heat-transfer rates and the time required to equilibrate the relatively large thermal mass of the substrate/tooling. Once the setpoint is held, the measured temperature approaches a quasi-steady plateau and tracks the isothermal segments more closely. Figure 5 (green symbols, right y-axis) shows the model-predicted conversion, $\alpha(t)$, calculated based on the measured temperature history, that is, the actual cure temperature. The predicted conversion remains near zero at early times and then increases sharply during the initial ramp, reaching ≈0.94 by the end of the first dwell. During the second ramp and hold (post-cure), further curing proceeds toward completion, with α rising to ≈0.99. The conversion remains essentially constant during the subsequent cooldown. This model-based prediction is important for underfill materials used in advanced electronic packaging, where insufficient cure or inaccurate cure-path assumptions can directly affect reliability, residual stress development, and long-term performance.

3.4 | Thermal Stability of Cured Underfill

Thermal degradation of polymeric materials is strongly governed by chemical composition and temperature and typically involves mass loss accompanied by the release of volatile degradation products [39]. Figure S6 shows dynamic TGA results for the cured underfill samples prepared as single, razor-blade–cut pieces ("hand-cut bulk") at different heating rates. While the overall degradation behavior is qualitatively similar across runs, the residual mass exhibited noticeable variability, which is attributed to the sensitivity of TGA to sample shape and surface-to-volume ratio [40].

To minimize these artifacts and improve sample uniformity, the hand-cut bulk specimens were subsequently cryomilled into a fine powder for the dynamic TGA measurements. Cryomilling is widely used for material homogenization in the pharmaceutical industry as well as in thermoplastic or polymer nanocomposite processing [41, 42]. This approach follows common TGA guidance that powdered or granular specimens with a high surface-to-volume ratio are preferred for better specimen-to-specimen uniformity [20]. In crosslinked thermosets (such as this underfill), which do not melt and flow during heating, specimen geometry can strongly influence the apparent mass-loss profile because thermal gradients are larger, and the diffusion and escape of volatile products are more limited in compact or thicker pieces. As a result, repeat TGA runs on different cryomilled samples yielded highly consistent results (Figure S7), demonstrating that improved sample homogeneity and reduced heat- and mass-transfer limitations improve measurement reproducibility. Cryomilling substantially increases the surface area of the material. With a median particle size (D50) of 4.2 μm from the volume-weighted distribution (Figure S8), the resulting powder is more susceptible to moisture uptake; therefore, a pre-drying step was used prior to the dynamic TGA scans (Experimental). The mass loss at the end of this step is 0.34% ± 0.04% (Table S2).

Cryomilling is expected to homogenize the composite material without altering its chemical characteristics. FTIR-ATR was used to investigate the effect of cryomilling on the chemical structure of the cured underfill. As shown in Figure S9, the spectra of the hand-cut bulk and cryomilled powder samples overlap closely across the measured range, with no new bands, band losses, or significant peak shifts detected within the measurement sensitivity. The dominant absorptions are consistent with a silica-filled epoxy network, including strong Si—O—Si stretching in the ≈1000–1200 cm^{-1} region as well as organic matrix features such as aromatic or aliphatic C—H stretching near ≈2800–3000 cm^{-1}, a carbonyl peak at 1728 cm^{-1}, and aromatic-, amine-, and ether-related bands in the fingerprint region (aromatic-ring bands and primary amine bands at 1600–1500 cm^{-1} and 900–650 cm^{-1}, and the ether/C—O—C region around 1100 cm^{-1} which is likely obscured due to the large Si—O—Si peaks) [43]. The near-identical appearance of these bands indicates that cryomilling does not introduce detectable changes in the chemical structure of the cured underfill. Previous work has also shown that cryomilling does not affect the chemical structure and crosslinking of cured structural composites, that is, carbon fiber-reinforced polymer (CFRP) thermoset prepreg, enabling thermal analysis techniques (DSC and TGA) to provide improved reproducibility and accuracy in measurements of the degree of cure and resin content [44].

The dynamic TGA/DTG results for the cryomilled samples are shown in Figure 6. The cryomilled sample still retained some moisture after pre-drying, as indicated by the small peak in the DTG curve below 100°C. The TGA curves exhibit a dominant primary mass loss event with a corresponding main DTG peak, followed by a slower, more gradual mass loss at higher temperatures. As expected for kinetically controlled degradation under non-isothermal conditions, increasing β shifts the mass loss transition to higher temperatures. The DTG peak temperature (maximum rate of mass loss) also increases with β, rising from 348°C at 1 K min^{-1} to 400°C at

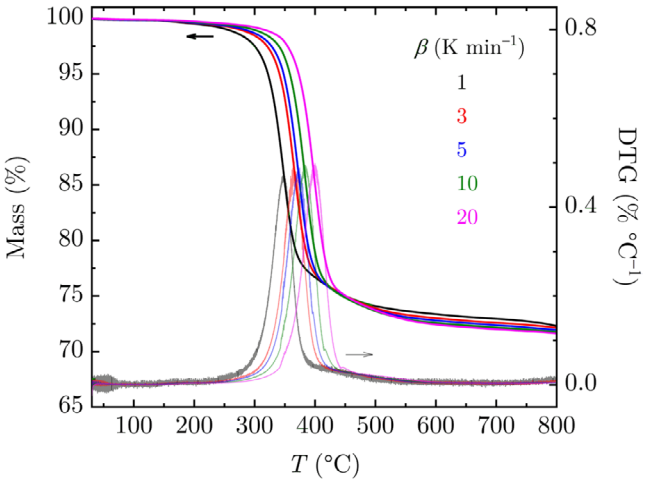

FIGURE 6 | Dynamic thermogravimetric analysis (TGA) mass (%) as a function of temperature for the cryomilled, cured underfill sample measured in N_2 at different heating rates (β). Curves from left to right correspond to increasing β. The corresponding derivative thermogravimetry (DTG) curves are plotted on the right *y*-axis. View in color for best clarity.

TABLE 2 | Degradation temperatures of the cured underfill material[a,b].

β (K min^{-1})	T_{onset}	$T_{10\%}$	T_{peak}	Residual mass (%)
1	318.1	339.2	348.1	73.0
3	336.8	357.5	365.7	72.6
5	343.6	363.9	374.6	72.4
10	354.6	374.3	383.2	72.2
20	369.5	389.3	400.0	72.0

[a]Thermal degradation properties obtained from dynamic TGA results at different heating rates β (Figure 6) for cryogenic milled samples after the pre-drying step.
[b]T_{onset}, the intersection of the zero mass loss baseline and the tangent line through the maximum slope point (or the peak temperature of the DTG curve) of the main TGA curve; $T_{10\%}$, temperature at 10% mass loss; T_{peak}, peak temperature of the DTG curve; residual mass (%) is taken as the mass (%) at 700°C. Standard uncertainties *u* are $u(T_{onset}) = 0.8$°C, $u(T_{10\%}) = 0.7$°C, $u(T_{peak}) = 1.1$°C, and u(residual mass) = 0.02%, based on repeat measurements of three specimens at a constant heating rate.

20 K min^{-1}. Characteristic degradation temperatures, including T_{onset}, $T_{10\%}$, T_{peak}, and the residual mass, are summarized in Table 2. The primary degradation step occurs over ≈250°C–450°C, consistent with the range widely reported for cured diglycidyl ether of bisphenol A (DGEBA)–based epoxy networks materials under inert atmospheres, and is attributed to decomposition of the crosslinked epoxy structure [45–48]. The high-temperature residual mass is 72.4% ± 0.3% across heating rates, consistent with a highly filled epoxy underfill formulation in which the inorganic silica filler and any char yield of the polymer contribute to the residue. Underfill materials commonly incorporate high loadings of silica or other inorganic fillers (typically ≈50% mass fraction to 70% mass fraction) to control CTE, modulus, and rheology [6]. Neat (unfilled) DGEBA-type epoxies generally leave smaller residues under nitrogen (only a few % mass fraction to < 15% mass fraction), depending on network chemistry and additives [46, 48–50]. Although fillers can increase high-temperature mass retention through interactions with polymer-derived char [45–48], the ≈72% residue is primarily attributed to the inorganic filler content.

3.5 | Degradation Kinetics and Lifetime Prediction

Decomposition kinetic parameters were determined from dynamic TGA measurements using the data in Figure 6 beginning at 100°C to minimize the effects of residual moisture loss. A mass loss of 5% was used as the failure criterion [20]. The temperatures at 5% TGA conversion were determined (Figure S10) and used for ASTM E1641 analysis, a special case of the Ozawa–Flynn–Wall isoconversional method [51, 52]. Figure 7a shows the ASTM E1641 analysis of the dynamic TGA data. Linear regression of the data yielded the slope used to calculate the activation energy. Using the iterative ASTM E1641 procedure with tabulated Doyle approximation [53] values, the activation energy was calculated to be 133.7 ± 3.7 kJ mol^{-1}.

Figure 7b shows the thermal endurance prediction according to ASTM E1877 [21]:

$$\log(t_f) = \frac{E}{2.303RT} + \log\left(\frac{E}{100.4R\beta}\right) - 0.463\frac{E}{RT_f} \quad (8)$$

where t_f is the thermal endurance (or lifetime corresponding to a selected temperature), and T_f is the failure temperature corresponding to 5% mass loss used in Figure 7a. The shaded region in Figure 7b represents the uncertainty propagated from the standard uncertainty in the apparent activation energy. As expected, the estimated thermal endurance increases with decreasing temperature. For example, increasing the temperature from 100°C to 150°C decreases the calculated thermal endurance by a factor of approximately 162, from approximately 45 years to 102 days. We note that the predicted lifetime should be interpreted as an inert-atmosphere kinetic extrapolation based on the selected failure criterion and the assumptions underlying the ASTM E1641/E1877 methods, rather than as a direct prediction of service lifetime. Specifically, the analysis applies a single apparent activation energy at a selected 5% mass-loss level, although the overall degradation process exhibits a multi-step degradation profile (Figure 6). In addition, the measurements were performed under nitrogen, whereas degradation during service may involve oxygen and other environmental factors. The calculation extrapolates below the experimental decomposition-temperature range and has not been correlated with long-term aging or field-service data. The results are therefore most appropriately used to compare the relative temperature sensitivity of degradation under the specified inert-atmosphere conditions.

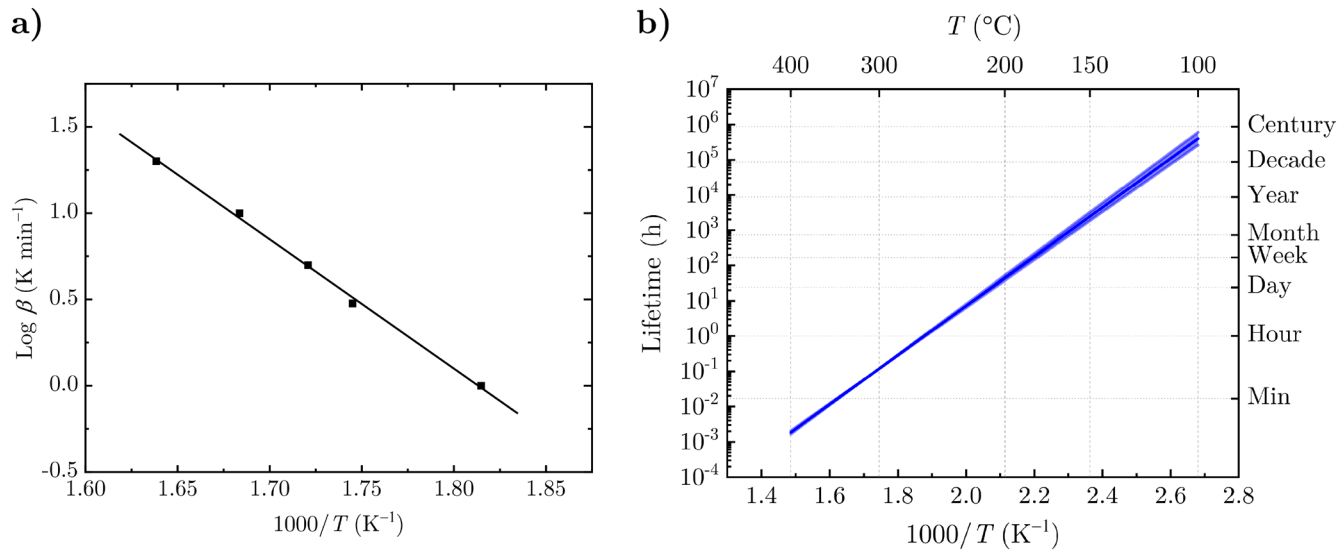

FIGURE 7 | (a) ASTM E1641 analysis of dynamic TGA data at 5% mass loss, showing the logarithm of heating rate as a function of 1000/*T*, with the solid line indicating the linear fit; (b) temperature-dependent thermal endurance estimates calculated from ASTM E1877 using the kinetic parameters obtained by ASTM E1641. The shaded region represents the uncertainty propagated from $u(E) = 3.7$ kJ mol^{-1}. The estimates correspond to a 5% mass-loss criterion under nitrogen and should be interpreted as inert-atmosphere kinetic extrapolations. The top *x*-axis shows decreasing temperature in °C, and the right *y*-axis indicates approximate lifetime in conventional time units.

4 | Conclusion

This work provides a practical and quantitatively grounded framework for evaluating cure evolution and long-term thermal durability of highly filled epoxy underfill materials used in advanced semiconductor packaging. Dynamic DSC results show that the curing behavior cannot be described as a single-step process. Combined isoconversional analysis and model fitting reveal a multistep curing mechanism, with diffusion limitations becoming increasingly important at high conversion. A two-step modified Kamal–Sourour model incorporating diffusion-controlled kinetics in the second step successfully described the curing process over the full conversion range, including the late-stage vitrification effects important for process-relevant prediction.

Cryomilling improved the reproducibility of TGA measurements by improving sample uniformity and reducing heat- and mass-transfer limitations, without causing detectable chemical changes in the cured material, thereby enabling more reliable thermal degradation analysis. The cured underfill exhibited a primary degradation process typical of epoxy networks and a high residual mass consistent with its highly filled composition. ASTM E1641 and E1877 analysis provided temperature-dependent estimates of thermal endurance, highlighting the strong sensitivity of projected lifetime to service temperature.

Overall, these results establish a practical basis for predicting cure progression and degradation based on thermal endurance estimation, supporting cure schedule optimization and thermal stability assessment for highly filled thermosetting materials used in industrial applications.

Acknowledgments

This work was performed with funding from the CHIPS Metrology Program, part of CHIPS for America, National Institute of Standards and Technology, U.S. Department of Commerce. R.T. acknowledges the National Institute of Standards and Technology (NIST), the U.S. Department of Commerce, for funding (Award # 70NANB24H283). R.G. is supported by the NIST Summer Undergraduate Research Fellowship (SURF) program. R.T. and R.G. acknowledge Debbie Jacobs and Dr. Xiaohong Gu of the NIST Engineering Laboratory for providing access to a TGA while their instrument was out of service. The statements, findings, conclusions, and recommendations are those of the authors and do not necessarily reflect the view of NIST or the U.S. Department of Commerce. Identification of a commercial product does not imply recommendation or endorsement by NIST nor does it imply that the product is necessarily the best for the stated purpose.

Funding

This work was supported by the National Institute of Standards and Technology (70NANB24H283).

Conflicts of Interest

Dr. Elena Moukhina is an employee of NETZSCH-Gerätebau GmbH, the developer of the Netzsch Kinetics Neo software used for the kinetic modeling in this study. The other authors declare no conflicts of interest.

Data Availability Statement

Data associated with this paper are publicly available through the NIST Public Data Repository at https://doi.org/10.18434/mds2-4162.

Endnotes

[1] Certain equipment, instruments, software, or materials are identified in this paper to specify the experimental procedure adequately. Such identification is not intended to imply recommendation or endorsement of any product or service by NIST, nor is it intended to imply that the materials or equipment identified are necessarily the best available for the purpose.

References

1. Z. Zhang, P. Zhu, and C. P. Wong, "Flip-Chip Underfill: Materials, Process, and Reliability," in *Materials for Advanced Packaging*, ed. D. Lu and C. P. Wong (Springer International Publishing, 2017), 331–371, https://doi.org/10.1007/978-3-319-45098-8_8.

2. T. Vidil, F. Tournilhac, S. Musso, A. Robisson, and L. Leibler, "Control of Reactions and Network Structures of Epoxy Thermosets," *Progress in Polymer Science* 62 (2016): 126–179, https://doi.org/10.1016/j.progpolymsci.2016.06.003.

3. P. Prasatya, G. B. McKenna, and S. L. Simon, "A Viscoelastic Model for Predicting Isotropic Residual Stresses in Thermosetting Materials: Effects of Processing Parameters," *Journal of Composite Materials* 35, no. 10 (2001): 826–848, https://doi.org/10.1177/a037322.

4. J. D. Russell, M. S. Madhukar, M. S. Genidy, and A. Y. Lee, "A New Method to Reduce Cure-Induced Stresses in Thermoset Polymer Composites, Part III: Correlating Stress History to Viscosity, Degree of Cure, and Cure Shrinkage," *Journal of Composite Materials* 34, no. 22 (2000): 1926–1947, https://doi.org/10.1106/UY9U-F2QW-2FKK-91KG.

5. Z. Plachý, J. Uřičář, D. Froš, A. Pražanová, K. Dušek, and A. Géczy, "Impact of Curing Profiles on the Thermo-Mechanical Properties of an Underfill in Board-Level Microelectronic Packaging: Effect on Reliability," *Composites Part A: Applied Science and Manufacturing* 200 (2026): 109298, https://doi.org/10.1016/j.compositesa.2025.109298.

6. R. Tao, P. Centellas, S. Romberg, et al., "Material Needs and Measurement Challenges for Advanced Semiconductor Packaging: Understanding the Soft Side of Science," *IEEE Transactions on Components, Packaging and Manufacturing Technology* 15, no. 10 (2025): 2071–2082, https://doi.org/10.1109/TCPMT.2025.3603484.

7. R. Tao, S. P. Phansalkar, A. M. Forster, and B. Han, "Investigation of Cure Kinetics of Advanced Epoxy Molding Compound Using Dynamic Heating Scan: An Overlooked Second Reaction," in *2023 IEEE 73rd Electronic Components and Technology Conference (ECTC)* (IEEE, 2023), 1319–1326, https://doi.org/10.1109/ECTC51909.2023.00225.

8. S. P. Phansalkar, Y. Jang, B. Han, R. Tao, and A. M. Forster, "Novel Method to Determine Autocatalytic Cure Kinetics Model Constants of Dual-Reaction Thermosets," *Materials Science and Engineering B* 311 (2025): 117829, https://doi.org/10.1016/j.mseb.2024.117829.

9. A. P. Kotula, R. Tao, J. Tu, Y. J. Lee, and G. A. Holmes, "Advanced Characterization of the Cure Kinetics of a Liquid Encapsulant," in *2025 IEEE 75th Electronic Components and Technology Conference (ECTC)* (IEEE, 2025), 1784–1790, https://doi.org/10.1109/ECTC51687.2025.00303.

10. P. Centellas, S. Romberg, R. Tao, et al., "Advanced Metrology Suite for Linking Residual Stress to Fundamental Properties of Thermoset Packaging Materials," in *2025 IEEE 75th Electronic Components and Technology Conference (ECTC)* (IEEE, 2025), 432–439, https://doi.org/10.1109/ECTC51687.2025.00078.

11. S. Vyazovkin, A. K. Burnham, J. M. Criado, L. A. Pérez-Maqueda, C. Popescu, and N. Sbirrazzuoli, "ICTAC Kinetics Committee Recommendations for Performing Kinetic Computations on Thermal Analysis Data," *Thermochimica Acta* 520, no. 1 (2011): 1–19, https://doi.org/10.1016/j.tca.2011.03.034.

12. S. Vyazovkin and N. Sbirrazzuoli, "Kinetic Methods to Study Isothermal and Nonisothermal Epoxy-Anhydride Cure," *Macromolecular Chemistry and Physics* 200, no. 10 (1999): 2294–2303, https://doi.org/10.1002/(SICI)1521-3935(19991001)200:10%253C2294::AID-MACP2294%253E3.0.CO;2-V.

13. D. Santiago, X. Fernández-Francos, X. Ramis, J. M. Salla, and M. Sangermano, "Comparative Curing Kinetics and Thermal–Mechanical Properties of DGEBA Thermosets Cured With a Hyperbranched Poly(Ethyleneimine) and an Aliphatic Triamine," *Thermochimica Acta* 526, no. 1 (2011): 9–21, https://doi.org/10.1016/j.tca.2011.08.016.

14. C. Strasser, E. Moukhina, and J. Hartmann, "Time–Temperature-Transformation (TTT) Cure Diagram of an Epoxy–Amine System," *Macromolecular Theory and Simulations* 33, no. 6 (2024): 2400039, https://doi.org/10.1002/mats.202400039.

15. P. I. Karkanas and I. K. Partridge, "Cure Modeling and Monitoring of Epoxy/Amine Resin Systems. I. Cure Kinetics Modeling," *Journal of Applied Polymer Science* 77, no. 7 (2000): 1419–1431, https://doi.org/10.1002/1097-4628(20000815)77:7%253C1419::AID-APP3%253E3.0.CO;2-N.

16. G. Wisanrakkit and J. K. Gillham, "The Glass Transition Temperature (Tg) as an Index of Chemical Conversion for a High-Tg Amine/Epoxy System: Chemical and Diffusion-Controlled Reaction Kinetics," *Journal of Applied Polymer Science* 41, no. 11–12 (1990): 2885–2929, https://doi.org/10.1002/app.1990.070411129.

17. J. P. Pascault and R. J. J. Williams, "Glass Transition Temperature Versus Conversion Relationships for Thermosetting Polymers," *Journal of Polymer Science Part B: Polymer Physics* 28, no. 1 (1990): 85–95, https://doi.org/10.1002/polb.1990.090280107.

18. T. Braun, K.-F. Becker, M. Koch, V. Bader, R. Aschenbrenner, and H. Reichl, "High-Temperature Reliability of Flip Chip Assemblies," *Microelectronics Reliability* 46, no. 1 (2006): 144–154, https://doi.org/10.1016/j.microrel.2005.06.004.

19. R. B. Prime, H. E. Bair, S. Vyazovkin, P. K. Gallagher, and A. Riga, "Thermogravimetric Analysis (TGA)," in *Thermal Analysis of Polymers* (John Wiley & Sons, Inc., 2009), 241–317, https://doi.org/10.1002/9780470423837.ch3.

20. "ASTM E1641-23 Standard Test Method for Decomposition Kinetics by Thermogravimetry Using the Ozawa/Flynn/Wall Method," https://doi.org/10.1520/E1641-23.

21. "ASTM E1877-21 Standard Practice for Calculating Thermal Endurance of Materials From Thermogravimetric Decomposition Data," https://doi.org/10.1520/E1877-21.

22. I. Blanco, "Application of Thermal Analysis Methods for Lifetime Prediction," in *Thermal Analysis of Polymeric Materials: Methods and Developments* (Wiley-VCH, 2022), 509–532, https://doi.org/10.1002/9783527828692.ch15.

23. R. Tao, F. Zhang, H. G. Nguyen, et al., "Temperature-Insensitive Silicone Composites as Ballistic Witness Materials: The Impact of Water Content on the Thermophysical Properties," *Journal of Materials Science* 56, no. 29 (2021): 16362–16375, https://doi.org/10.1007/s10853-021-06334-x.

24. S. Vyazovkin, A. K. Burnham, L. Favergeon, et al., "ICTAC Kinetics Committee Recommendations for Analysis of Multi-Step Kinetics," *Thermochimica Acta* 689 (2020): 178597, https://doi.org/10.1016/j.tca.2020.178597.

25. H. L. Friedman, "Kinetics of Thermal Degradation of Char-Forming Plastics From Thermogravimetry. Application to a Phenolic Plastic," *Journal of Polymer Science Part C: Polymer Symposia* 6, no. 1 (1964): 183–195, https://doi.org/10.1002/polc.5070060121.

26. C. Lu, W. Song, and W. Lin, "Kinetics of Biomass Catalytic Pyrolysis," *Biotechnology Advances* 27, no. 5 (2009): 583–587, https://doi.org/10.1016/j.biotechadv.2009.04.014.

27. E. Moukhina, "Initial Kinetic Parameters for the Model-Based Kinetic Method," *High Temperatures-High Pressures* 42, no. 4 (2013): 287–302.

28. J. R. Opfermann, E. Kaisersberger, and H. J. Flammersheim, "Model-Free Analysis of Thermoanalytical Data-Advantages and Limitations," *Thermochimica Acta* 391, no. 1 (2002): 119–127, https://doi.org/10.1016/S0040-6031(02)00169-7.

29. E. Franieck, M. Fleischmann, O. Hölck, L. Kutuzova, and A. Kandelbauer, "Cure Kinetics Modeling of a High Glass Transition Temperature Epoxy Molding Compound (EMC) Based on Inline Dielectric Analysis," *Polymers* 13, no. 11 (2021): 1734, https://doi.org/10.3390/polym13111734.

30. G. Van Assche, S. Swier, and B. Van Mele, "Modeling and Experimental Verification of the Kinetics of Reacting Polymer Systems," *Thermochimica Acta* 388, no. 1 (2002): 327–341, https://doi.org/10.1016/S0040-6031(02)00038-2.

31. M. R. Kamal and S. Sourour, "Kinetics and Thermal Characterization of Thermoset Cure," *Polymer Engineering & Science* 13, no. 1 (1973): 59–64, https://doi.org/10.1002/pen.760130110.

32. J. B. Enns and J. K. Gillham, "Time–Temperature–Transformation (TTT) Cure Diagram: Modeling the Cure Behavior of Thermosets," *Journal of Applied Polymer Science* 28, no. 8 (1983): 2567–2591, https://doi.org/10.1002/app.1983.070280810.

33. S. Vyazovkin, D. Achilias, X. Fernandez-Francos, A. Galukhin, and N. Sbirrazzuoli, "ICTAC Kinetics Committee Recommendations for Analysis of Thermal Polymerization Kinetics," *Thermochimica Acta* 714 (2022): 179243, https://doi.org/10.1016/j.tca.2022.179243.

34. J. E. K. Schawe, "A Description of Chemical and Diffusion Control in Isothermal Kinetics of Cure Kinetics," *Thermochimica Acta* 388, no. 1 (2002): 299–312, https://doi.org/10.1016/S0040-6031(02)00041-2.

35. S. L. Simon and J. K. Gillham, "Cure Kinetics of a Thermosetting Liquid Dicyanate Ester Monomer/High-Tg Polycyanurate Material," *Journal of Applied Polymer Science* 47, no. 3 (1993): 461–485, https://doi.org/10.1002/app.1993.070470308.

36. E. Rabinowitch, "Collision, co-Ordination, Diffusion and Reaction Velocity in Condensed Systems," *Transactions of the Faraday Society* 33 (1937): 1225–1233.

37. M. L. Williams, R. F. Landel, and J. D. Ferry, "The Temperature Dependence of Relaxation Mechanisms in Amorphous Polymers and Other Glass-Forming Liquids," *Journal of the American Chemical Society* 77, no. 14 (1955): 3701–3707.

38. L. E. Nielsen, "Cross-Linking–Effect on Physical Properties of Polymers," *Journal of Macromolecular Science, Part C* 3, no. 1 (1969): 69–103, https://doi.org/10.1080/15583726908545897.

39. J. H. Flynn, "Chapter 14 - Polymer Degradation," in *Handbook of Thermal Analysis and Calorimetry*, vol. 3, ed. S. Z. D. Cheng (Elsevier Science B.V., 2002), 587–651, https://doi.org/10.1016/S1573-4374(02)80017-6.

40. V.-M. Archodoulaki, T. Koch, and M. P. Jones, "Thermo(Oxidative) Stability of Polymeric Materials," in *Thermal Analysis of Polymeric Materials: Methods and Developments* (Wiley-VCH, 2022), 353–379, https://doi.org/10.1002/9783527828692.ch9.

41. F. Delogu, G. Gorrasi, and A. Sorrentino, "Fabrication of Polymer Nanocomposites via Ball Milling: Present Status and Future Perspectives," *Progress in Materials Science* 86 (2017): 75–126, https://doi.org/10.1016/j.pmatsci.2017.01.003.

42. N. Chieng, T. Rades, and J. Aaltonen, "An Overview of Recent Studies on the Analysis of Pharmaceutical Polymorphs," *Journal of Pharmaceutical and Biomedical Analysis* 55, no. 4 (2011): 618–644, https://doi.org/10.1016/j.jpba.2010.12.020.

43. R. M. Silverstein, G. C. Bassler, and T. C. Morrill, *Spectrometric Identification of Organic Compounds*, Fifth ed. (John Wiley and Sons, Inc., 1991).

44. N. Fereshteh-Saniee, N. Reynolds, C. A. Kelly, P. R. Wilson, M. J. Jenkins, and K. N. Kendall, "Introducing Cryomilling for Reliable Determination of Resin Content and Degree of Cure in Structural Carbon Fibre Reinforced Thermoset Composites," *Composites Part A: Applied Science and Manufacturing* 107 (2018): 197–204, https://doi.org/10.1016/j.compositesa.2018.01.004.

45. Y.-L. Liu, W.-L. Wei, K.-Y. Hsu, and W.-H. Ho, "Thermal Stability of Epoxy-Silica Hybrid Materials by Thermogravimetric Analysis," *Thermochimica Acta* 412, no. 1 (2004): 139–147, https://doi.org/10.1016/j.tca.2003.09.004.

46. F.-L. Jin and S.-J. Park, "Thermal Properties of Epoxy Resin/Filler Hybrid Composites," *Polymer Degradation and Stability* 97, no. 11 (2012): 2148–2153, https://doi.org/10.1016/j.polymdegradstab.2012.08.015.

47. V. D'Eusanio, A. G. Rombolà, I. Coralli, D. Fabbri, L. Tassi, and A. Marchetti, "Thermal Degradation Pathways in Multi-Component Epoxy Composites," *Journal of Analytical and Applied Pyrolysis* 189 (2025): 107107, https://doi.org/10.1016/j.jaap.2025.107107.

48. J. Macan, H. Ivankovic, M. Ivankovic, and H. J. Mencer, "Synthesis and Characterization of Organic–Inorganic Hybrids Based on Epoxy Resin and 3-Glycidyloxypropyltrimethoxysilane," *Journal of Applied Polymer Science* 92, no. 1 (2004): 498–505, https://doi.org/10.1002/app.20024.

49. S.-J. Park, H.-C. Kim, H.-I. Lee, and D.-H. Suh, "Thermal Stability of Imidized Epoxy Blends Initiated by N-Benzylpyrazinium Hexafluoroantimonate Salt," *Macromolecules* 34, no. 22 (2001): 7573–7575, https://doi.org/10.1021/ma010792x.

50. S.-P. Rwei, S.-C. Kao, G.-S. Liou, K.-C. Cheng, and W. Guo, "Curing and Pyrolysis of Epoxy Resins Containing 2-(6-Oxido-6H-Dibenz(c,e)(1,2)Oxaphosphorin-6-Yl)-1,4-Naphthalenediol or Bisphenol S," *Colloid and Polymer Science* 281, no. 5 (2003): 407–415, https://doi.org/10.1007/s00396-002-0787-8.

51. J. H. Flynn and L. A. Wall, "A Quick, Direct Method for the Determination of Activation Energy From Thermogravimetric Data," *Journal of Polymer Science Part B: Polymer Letters* 4, no. 5 (1966): 323–328, https://doi.org/10.1002/pol.1966.110040504.

52. T. Ozawa, "A New Method of Analyzing Thermogravimetric Data," *Bulletin of the Chemical Society of Japan* 38, no. 11 (1965): 1881–1886, https://doi.org/10.1246/bcsj.38.1881.

53. C. D. Doyle, "Kinetic Analysis of Thermogravimetric Data," *Journal of Applied Polymer Science* 5, no. 15 (1961): 285–292, https://doi.org/10.1002/app.1961.070051506.

Supporting Information

Additional supporting information can be found online in the Supporting Information section. **Figure S1:** An enlarged view of the dynamic DSC heat flow curves shown in Figure 1 for the uncured underfill material, measured at different heating rates (β). Heat flow ($\dot{Q}$) is scaled by (β_{ref}/β), where β_{ref} is 10 K min^{-1}. The area under the 0.6 K min^{-1} curve is filled for visual distinction. **Figure S2:** Example DSC heat flow curve from the second heating scan for the underfill following the first heating scan at $\beta = 10\,\text{min}^{-1}$. The vertical dashed line indicates the glass transition temperature for the fully cured material. **Figure S3:** Conversion rate ($d\alpha/dt$) as a function of temperature for the underfill material at heating rates of 0.6 K min^{-1} and 1 K min^{-1}. An enlarged view is shown to better evaluate the goodness of fit. Symbols represent experimental data obtained from dynamic DSC, while solid lines represent predictions of a two-step autocatalytic model without diffusion-controlled kinetics (Equations 2 and 3). **Figure S4:** Glass transition temperature as a function of conversion. The line represents a fit to the DiBenedetto equation (Equation 7) with the T_g values for the uncured material ($T_{g0} = -47.5$°C) and fully cured material ($T_{g\infty} = 171.0$°C) shown as open and filled circles, respectively, with $\lambda = 0.4$. **Figure S5:** Conversion rate ($d\alpha/dt$) as a function of temperature for the underfill material at heating rates of 0.6 K min^{-1} and 1 K min^{-1}. An enlarged view is shown to better evaluate the goodness of fit. Symbols represent experimental data obtained from dynamic DSC, while solid lines represent predictions of a two-step autocatalytic model (Equations 2 and 3) with diffusion control included in the second step (Equations 4–7). **Figure S6:** Dynamic thermogravimetric analysis (TGA) mass (%) as a function of temperature for a single-piece cured underfill sample measured in N_2 at different heating rates (β). **Figure S7:** Dynamic TGA (solid lines, left y-axis) and DTG (dotted lines, right y-axis) curves for three specimens of the cryomilled, cured underfill powder measured at a heating rate (β) of 10 K min^{-1}. **Figure S8:** Volume-based particle size distribution Q_v (% volume fraction) as a function of particle diameter (μm) for the cryomilled underfill sample. The median diameter D50 ≈ (4.2 ± 0.1) μm. **Figure S9:** Representative Fourier transform infrared (FTIR) spectra of the cured underfill prepared as a hand-cut bulk piece (black) and as a cryomilled powder (red). Spectra are shown in two wavenumber windows (4000 to 2500) cm^{-1} and (1900 to 600) cm^{-1} to highlight key vibrational bands. **Figure S10:** TGA conversion (α) versus temperature for dynamic heating rates of (1, 3, 5, 10, 20, and) K min^{-1}. The degree of conversion for TGA is the ratio of the current mass loss to the total mass loss. The dashed vertical lines indicate the temperatures at 5% conversion used for ASTM E1641 analysis. **Table S1:** Kinetic parameters for a two-step modified Kamal–Sourour model without diffusion control. **Table S2:** Mass loss (%) of the cryogenic milled samples after the pre-drying step in TGA.